

# SDSS J0246–0825: A New Gravitationally Lensed Quasar from the Sloan Digital Sky Survey<sup>1</sup>

Naohisa Inada,<sup>2</sup> Scott Burles,<sup>3</sup> Michael D. Gregg,<sup>4,5</sup> Robert H. Becker,<sup>4,5</sup> Paul L. Schechter,<sup>3</sup> Daniel J. Eisenstein,<sup>6</sup> Masamune Oguri,<sup>7,8</sup> Francisco J. Castander,<sup>9</sup> Patrick B. Hall,<sup>10</sup> David E. Johnston,<sup>8</sup> Bartosz Pindor,<sup>11</sup> Gordon T. Richards,<sup>8</sup> Donald P. Schneider,<sup>12</sup> Richard L. White,<sup>13</sup> J. Brinkmann,<sup>14</sup> Alexander S. Szalay,<sup>15</sup> and Donald G. York<sup>16,17</sup>

## ABSTRACT

---

<sup>1</sup>Based on observations with the NASA/ESA *Hubble Space Telescope*, obtained at the Space Telescope Science Institute, which is operated by the Association of Universities for Research in Astronomy, Inc., under NASA contract NAS 5-26555. These observations are associated with *HST* program 9744.

<sup>2</sup>Institute of Astronomy, Faculty of Science, University of Tokyo, 2-21-1 Osawa, Mitaka, Tokyo 181-0015, Japan.

<sup>3</sup>Physics Department, Massachusetts Institute of Technology, 77 Massachusetts Avenue, Cambridge, MA 02139.

<sup>4</sup>IGPP-LLNL, L-413, 7000 East Avenue, Livermore, CA 94550.

<sup>5</sup>Physics Department, University of California, Davis, CA 95616.

<sup>6</sup>Steward Observatory, University of Arizona, 933 North Cherry Avenue, Tucson, AZ 85721.

<sup>7</sup>Department of Physics, University of Tokyo, Hongo 7-3-1, Bunkyo-ku, Tokyo 113-0033, Japan.

<sup>8</sup>Princeton University Observatory, Peyton Hall, Princeton, NJ 08544.

<sup>9</sup>Institut d'Estudis Espacials de Catalunya/CSIC, Gran Capita 2-4, 08034 Barcelona, Spain.

<sup>10</sup>Department of Physics & Astronomy, York University, 4700 Keele St., Toronto, ON M3J 1P3, Canada.

<sup>11</sup>Department of Astronomy, University of Toronto, 60 St. George Street, Toronto, Ontario M5S 3H8, Canada.

<sup>12</sup>Department of Astronomy and Astrophysics, The Pennsylvania State University, 525 Davey Laboratory, University Park, PA 16802.

<sup>13</sup>Space Telescope Science Institute, 3700 San Martin Drive, Baltimore, MD 21218.

<sup>14</sup>Apache Point Observatory, P.O. Box 59, Sunspot, NM 88349.

<sup>15</sup>Center for Astrophysical Sciences, Department of Physics & Astronomy, Johns Hopkins University, Baltimore, MD 21218.

<sup>16</sup>Department of Astronomy and Astrophysics, The University of Chicago, 5640 South Ellis Avenue, Chicago, IL 60637.

<sup>17</sup>Enrico Fermi Institute, The University of Chicago, 5640 South Ellis Avenue, Chicago, IL 60637.

We report the discovery of a new two-image gravitationally lensed quasar, SDSS J024634.11–082536.2 (SDSS J0246–0825). This object was selected as a lensed quasar candidate from the Sloan Digital Sky Survey (SDSS) by the same algorithm that was used to discover other SDSS lensed quasars (e.g., SDSS J0924+0219). Multicolor imaging with the Magellan Consortium’s Walter Baade 6.5-m telescope and the spectroscopic observations using the W. M. Keck Observatory’s Keck II telescope confirm that SDSS J0246–0825 consists of two lensed images ( $\Delta\theta = 1''.04$ ) of a source quasar at  $z = 1.68$ . Imaging observations with the Keck telescope and the *Hubble Space Telescope* reveal an extended object between the two quasar components, which is likely to be a lensing galaxy of this system. From the absorption lines in the spectra of quasar components and the apparent magnitude of the galaxy, combined with the expected absolute magnitude from the Faber-Jackson relation, we estimate the redshift of the lensing galaxy to be  $z = 0.724$ . A highly distorted ring is visible in the *Hubble Space Telescope* images, which is likely to be the lensed host galaxy of the source quasar. Simple mass modeling predicts the possibility that there is a small (faint) lensing object near the primary lensing galaxy.

*Subject headings:* gravitationally lensing — quasars: individual (SDSS J024634.11–082536.2)

## 1. Introduction

Since the discovery of the first lensed quasar, Q0957+561 (Walsh, Carswell, & Weymann 1979), approximately 80 lensed quasars have been discovered to date. Gravitationally lensed quasars are now known to be an useful tool for cosmology and astrophysics, such as measurements of dark energy (Turner 1990; Fukugita, Futamase, & Kasai 1990; Chiba & Yoshii 1999; Chae et al. 2002), direct probes of the Hubble constant (Refsdal 1964; Bernstein & Fischer 1999; Koopmans et al. 2003), and the study of lensing galaxies (Kochanek 1991; Keeton 2001a; Oguri 2002; Koopmans & Treu 2003; Rusin, Kochanek, & Keeton 2003; Ofek, Rix, & Maoz 2003). In order to use lensed quasars as these cosmological and astrophysical tests, large and homogeneous samples of gravitational lenses are necessary, either to ensure good statistical precisions and to provide sufficient number of lensing systems which are suitable for measurements of time delays and/or for studies of the lensing galaxies. Although several previous large and homogeneous lensed quasar surveys, e.g., Jodrell/VLA Astrometric Survey and the Cosmic Lens All-Sky Survey (Myers et al. 2003; Browne et al. 2003) and the *Hubble Space Telescope* Snapshot Survey (Maoz et al. 1992, 1993a,b; Bahcall et al. 1992), are of considerable value, discoveries of more lensed quasars in larger surveys, such

as the Sloan Digital Sky Survey (SDSS; York et al. 2000; Stoughton et al. 2002; Abazajian et al. 2003, 2004) will greatly improve the accuracy of these cosmological and astrophysical tests. The final number of spectroscopically confirmed quasars in the SDSS is expected to be about  $10^5$ , thus, if we assume the lensing rate of 0.1% (Turner, Ostriker, & Gott 1984), the expected number of gravitationally lensed quasars in the SDSS will be approximately  $10^2$ ; the SDSS could double the number of lensed quasars. Indeed, several newly discovered lensed quasars in the SDSS data have already been reported (Inada et al. 2003a,b,c; Morgan, Snyder, & Reens 2003; Johnston et al. 2003; Pindor et al. 2004; Oguri et al. 2004a,b).

In this paper, we report the discovery of another lensed quasar, SDSS J024634.11–082536.3 (SDSS J0246–0825). This object was selected as a lensed quasar candidate (an “extended” quasar) from about 50,000 SDSS quasars using the algorithm described in Inada et al. (2003b), Pindor et al. (2004), Oguri et al. (2004a) and Oguri et al. (2004b). Since the SDSS imaging and spectroscopic data of SDSS J0246–0825 are unresolved, we conducted additional observations using the W. M. Keck Observatory’s Keck II telescope, the Magellan Consortium’s Walter Baade 6.5-m telescope (WB6.5m)<sup>17</sup>, and the *Hubble Space Telescope* (*HST*). These observations demonstrate that SDSS J0246–0825 is a two-image lens (the image separation is  $1''.04$ ) of a source quasar at  $z = 1.68$ , and that the likely lensing galaxy has been detected.

The structure of this paper is as follows. Section 2 describes both the photometric and spectroscopic follow-up observations. In §3, we show mass modeling of this lensing system. Finally, we present a summary and give a conclusion in §4. We assume a Lambda-dominate cosmology (Spergel et al. 2003; matter density  $\Omega_M = 0.27$ , cosmological constant  $\Omega_\Lambda = 0.73$ , and the Hubble constant  $H_0 = 70 \text{ km sec}^{-1} \text{ Mpc}^{-1}$ ), and we use AB magnitude system (Oke & Gunn 1983; Fukugita et al. 1996) throughout the paper.

## 2. Follow-up Observation and Data Analysis

### 2.1. SDSS Observations

The SDSS is a project to conduct in parallel a photometric survey (Gunn et al. 1998; Lupton, Gunn, & Szalay 1999) and a spectroscopic survey (Blanton et al. 2003) of 10,000

---

<sup>17</sup>The first telescope of the Magellan Project; a collaboration between the Observatories of the Carnegie Institution of Washington (OCIW), University of Arizona, Harvard University, University of Michigan, and Massachusetts Institute of Technology (MIT) to construct two 6.5 Meter optical telescopes in the southern hemisphere.

square degrees of the sky centered approximately on the North Galactic Pole, using dedicated wide-field ( $3^\circ$  field of view) 2.5-m telescope at Apache Point Observatory in New Mexico, USA. The astrometric positions are accurate to better than about  $0''.1$  rms per coordinate (Pier et al. 2003) and the photometric errors are less than about 0.03 magnitude (Hogg et al. 2001; Smith et al. 2002; Ivezić et al. 2004). Photometric observations are conducted using five optical broad bands (Fukugita et al. 1996). After automated data processing by the photometric pipeline (Lupton et al. 2001), quasar, galaxy and luminous red galaxy candidates are selected by the target selection pipelines (Eisenstein et al. 2001; Richards et al. 2002; Strauss et al. 2002). Spectra of these candidates are obtained with a multi-fiber spectrograph covering  $3800 \text{ \AA}$  to  $9200 \text{ \AA}$  (resolution  $R \sim 1800$ ).

The *ugriz* SDSS images of SDSS J0246–0825 (sky and bias subtracted and flat-field corrected) are shown in Figure 1. Two stellar components are marginally-resolved/unresolved in the SDSS images; total magnitudes (in  $\sim 2''.0$  aperture radius) of the two quasar components and the lensing galaxy (and an unknown extended object, see below) are  $18.21 \pm 0.02$ ,  $17.99 \pm 0.01$ ,  $17.95 \pm 0.01$ ,  $17.60 \pm 0.01$ , and  $17.58 \pm 0.02$  in *u*, *g*, *r*, *i*, and *z*, respectively. These errors in the magnitudes are statistical errors. We show the field image (SDSS *i* band image) around SDSS J0246–0825, including a nearby star (star S) which is seen in both the WB6.5m images and the SDSS images, in Figure 2. We use star S to estimate a Point Spread Function (PSF) and to calibrate magnitudes. SDSS J0246–0825 was targeted as a quasar candidate by the target selection pipelines, and the spectrum was taken by the SDSS spectrograph. The spectrum data are also unresolved due to the spatial resolution of the SDSS spectroscopy, but it clearly shows the quasar emission lines at  $z = 1.686 \pm 0.001$ .

## 2.2. Follow-up Observation using the Walter Baade Telescope

High-resolution images of SDSS J0246–0825 in the *u*, *g*, *r*, and *i* filters were obtained with the Magellan Instant Camera (MagIC, a  $2048 \times 2048$  CCD camera; pixel scale is  $0''.069$ ) on the WB6.5m telescope, on 2002 February 13. The seeing (FWHM) was  $\sim 0''.5$ – $0''.6$ , and the exposure time was 120 sec in each band. The *u*, *g*, *r*, and *i* MagIC images of SDSS J0246–0825 are shown in Figure 3. Two stellar components are clearly seen in all these images; we named the two stellar components A and B, with A being the brighter component. The flux ratios between components B and A (estimated by the single Gaussian fit) are 0.32, 0.31, 0.33, and 0.34 in *u*, *g*, *r*, and *i*, respectively.

The PSFs derived from star S were subtracted from the original *i* band MagIC image. The peak flux and the center coordinates of components A and B in the MagIC *i* band image were calculated by the single Gaussian fit. The results agree with those obtained by

the imexamine task in IRAF<sup>18</sup>. The *i* band PSF-subtracted image is shown in the right panel of Figure 4. Although it is not obvious in Figure 4, we find a faint, extended object ( $\sim 21.8$  mag in  $0''.5$  aperture radius) between the two stellar components after the PSF subtraction. For further discussion of this object, see the Keck results in §2.3 and/or the *HST* results in §2.4. The angular separation (in the *i* band image) between components A and B is  $1''.042 \pm 0''.003$ . The *ugri* band PSF magnitudes of components A and B and the *i* band aperture magnitude of the extended objects between components A and B (component G, see below) are summarized in Table 1. Here we used star S (see Figure 2) as a photometric star<sup>19</sup>.

### 2.3. Follow-up Observation using the Keck Telescope

We conducted a near-infrared imaging observation of SDSS J0246–0825 using the Keck I telescope, on 2002 August 21. Although the night was not photometric, we obtained *K'* band data with the Near InfraRed Camera (NIRC; Matthews & Soifer 1994). The seeing (FWHM) was variable, averaging about  $0''.4$ , and the total exposure time was 900 sec. The deconvolved *K'* band image is shown in Figure 5; the deconvolution was done using the method which is described in Magain, Courbin, & Sohy (1998). The pixel size is half that of the raw image,  $0''.075$ . In Figure 5, we can clearly see an extended object (named component G) at the same position of the extended object found in the PSF-subtracted MagIC *i* band image (we can see component G more clearly in the PSF-subtracted images, the inset of Figure 5). This object is probably the lensing galaxy of this lensed quasar system; this hypothesis is further supported by the spectroscopic observation of the two stellar components using the Keck telescope and the high-resolution imaging observation using the *HST* (see §2.4). The flux ratio between components B and A is 0.29 in the *K'* band image; this is consistent with the mean flux ratio of the optical bands.

Spectra of the two components of SDSS J0246–0825 were acquired using the Keck II telescope on 2002 December 4. We conducted a spectroscopic follow-up observation using the Echellette Spectrograph and Imager (ESI; Sutin 1997; Sheinis et al. 2002) with the MIT-LL

---

<sup>18</sup>IRAF is the Image Reduction and Analysis Facility, a general purpose software system for the reduction and analysis of astronomical data. IRAF is written and supported by the IRAF programming group at the National Optical Astronomy Observatories (NOAO) in Tucson, Arizona. NOAO is operated by the Association of Universities for Research in Astronomy (AURA), Inc. under cooperative agreement with the National Science Foundation.

<sup>19</sup>Note that there are small (a few percent) differences between the filter response functions of the WB6.5m and those of the SDSS.

2048×4096 CCD camera. We used the Echellette mode. The spectral range covers 3900 Å to 11,000 Å, and the spectral resolution is  $R \simeq 27000$ . We set the slit width 1"0 and the slit orientation so that the two stellar components (components A and B; see Figure 3) were on the slit (thus, component G should be also on the slit, but we were not able to extract the spectrum of component G because it is much fainter than the quasar components). The exposure time was 900 sec. Since the seeing (FWHM) was about 0"7 and the angular separation between the two components is only 1"04, we can clearly see there are two objects on the slit but these are not well resolved. Therefore we extracted the spectra using a method of summing the fluxes in a window around the position of the brighter component and in another window shifted by 1"04. Sky was subtracted using neighboring windows on either side of the trace. There are bad columns on the ESI chip between 4460 Å and 4560 Å, and therefore, we excluded the data of this bad region from the spectra. The binned spectra of components A and B taken with ESI on Keck II are shown in Figure 6. In both spectra, C IV, C III], and Mg II emission lines are clearly seen at the same wavelength positions. The redshifts of components A and B are  $1.6820 \pm 0.0001$  and  $1.6816 \pm 0.0004$ , which were calculated by fitting the Voigt functions with the C IV emission lines. The velocity difference between the two quasar components is  $20 \text{ km sec}^{-1} \pm 40 \text{ km sec}^{-1}$ . The redshifts and the widths of the emission lines are summarized in Table 2. In addition to the identical redshift, the spectral energy distributions themselves are also quite similar. The bottom line in Figure 6 shows the spectral flux ratio between components B and A. We find that this is almost constant for a wide range of wavelengths and this is almost consistent with the mean flux ratio (0.33) of the *ugri* images. A large difference is seen around the C IV emission line; this might be caused by microlensing of the broad emission line region (Richards et al. 2004).

In addition to the emission lines, we found a Mg II/Mg I absorption system redshifted to  $z = 0.724$ , as shown in Figure 7. This absorption system probably arises from a lensing galaxy, both because galaxies can produce such Mg II absorption systems (Bergeron 1988; Bergeron & Boisse 1991) and because the Mg II/Mg I absorption system ( $z = 0.724$ ) is not so far from the half of the angular diameter distance to the quasar components ( $z = 1.688$ ) that has the maximum lensing efficiency (Ofek et al. 2003). This prediction is further supported by the comparison of the expected magnitude by the mass models with the observed magnitude of the lensing galaxy (see §3). Furthermore, we found two Mg II absorption systems, whose redshifts are 1.537 and 1.531 (both at  $\sim 7100$  Å), with their Fe II absorption lines (at  $\sim 6600$  Å,  $\sim 6000$  Å, and so on) and weaker absorption lines of other elements. Moreover, at  $\sim 7100$  Å, we found two possible Mg II absorption systems whose redshifts are 1.540 and 1.533, although their Fe II absorption lines and other element absorption lines were not detected in the spectra. However these 4 absorption systems are unlikely to be associated with the lensing system, because the difference between the redshift of the source quasar and that of

the absorption systems is small.

#### 2.4. Follow-up Observation using the *HST*

Our final observation of SDSS J0246–0825 was conducted using the *Hubble Space Telescope*, under the “*HST* Imaging of Gravitational Lenses” program (principal investigator: C. S. Kochanek, proposal ID: Cycle12–9744). We used the Advanced Camera for Surveys (ACS; Clampin 2000) and the Near Infrared Camera and Multi-Object Spectrometer (NICMOS; Thompson 1992), installed on the *HST*. The ACS and NICMOS observations were conducted on 2003 October 13 and 2003 December 18, respectively. We used F555W filter ( $\approx V$ -band) and the F814W filter ( $\approx I$ -band) in the ACS observation and the F160W filter ( $\approx H$ -band) in the NICMOS observation.

The ACS imaging observation consists of two dithered exposures taken in ACCUM mode. Total exposure time of each dithered exposure for the F555W filter was 1094 sec and that for the F814W filter was 1144 sec. The reduced (drizzled and calibrated) images were extracted using the CALACS calibration pipeline which includes the PyDrizzle algorithm. The combined image of the F555W filter and that of the F814W filter are shown in the left panels of Figure 8. As well as the NIRC  $K'$  band image (Figure 5), we find the extended object (component G) between the two quasar components in the ACS images, particularly in the F814W image. The extended nature and the red color of component G suggest that this object is a galaxy. In addition to the identical nature of the spectral energy distributions of components A and B (described in §2.3), the existence of the galaxy strongly supports the lensing hypothesis; we conclude that SDSS 0246–0825 is certainly a lensed quasar system. Although the spectrum of component G has not been obtained yet, the color of component G ( $V - I \approx 2.8$ , estimated from the PSF-subtracted images, the right panels of Figure 8) is consistent with it being a galaxy at  $z = 0.724$  (Fukugita, Shimasaku, & Ichikawa 1995), which is the redshift of Mg II/Mg I absorption system seen in the spectra of components A and B (see Figure 7).

In addition to the central extended object (component G), we find a highly distorted object (named component C) in the upper left of component A. Similar “ring” features of lensed (host) galaxies have been found in the optical and/or near-infrared band images (e.g., Impey et al. 1998; King et al. 1998; Warren et al. 1996), and therefore this object is probably the lensed host galaxy of the source quasar of SDSS 0246–0825. To improve the visibility of this distorted feature, we subtract components A and B using the quasar PSFs produced by the Tiny Tim software (version 6.1a; Krist & Hook 2003). The PSFs of quasars were constructed with the Keck spectra of components A and B. The result is shown in the right

panels of Figure 8. Component C is bright even in the F555W filter image as well as the F814W filter image (see Figure 8); the blue color of component C indicates that the host galaxy might be a starburst galaxy. The (magnification) center of component C is  $0''.50$  away from that of component A in the image plane, but the similar phenomenon have been observed in another lensed quasar system (Inada et al. 2005). See §3 for the comparison of this “ring” and mass models.

The NICMOS imaging observation consists of four dithered exposures taken in MULTIACCUM mode, through the F160W filter ( $\approx H$ -band). The exposure time was 640 sec for three dithered exposures and 704 sec for one dithered exposure. The reduced (calibrated) images were extracted using the CALNICA pipeline. The central bad columns of each dithered image were corrected by linear interpolation. The combined image is shown in the left panel of Figure 9. First, we confirm the existence of the central extended object (component G) between components A and B, and the highly distorted object (component C) near component A. In addition, we find a further highly distorted object, which is similar to component C, near component B in the F160W image. To improve the visibility of them, we subtract components A and B using the quasar PSFs produced by the Tiny Tim software. The PSF of a quasar was constructed with an  $\alpha_\nu = -0.5$  power law spectrum. The peak flux and the center coordinates of components A and B in the NICMOS F160W image were calculated using the imexamine task in IRAF. The result is shown in the right panel of Figure 9; one can clearly see the distorted objects form a nearly perfect ring. This prefect ring feature can be also seen in the PSF-subtracted NIRC  $K'$  band image (Figure 5). The PSF magnitudes of components A and B and the aperture magnitude of component G in F160W filter ( $\approx H$ -band) are summarized in Table 1. In estimating the aperture magnitude of component G, we used the aperture radius of  $0''.375$  in the PSF subtracted image.

### 3. Mass Modeling

We model the lensed quasar system using two mass models. One is the Singular Isothermal Sphere with external shear (SIS+shear) model, with a projected potential of

$$\psi(r, \theta) = \alpha_e r + \frac{\gamma}{2} r^2 \cos 2(\theta - \theta_\gamma), \quad (1)$$

where  $\alpha_e$  is the Einstein radius in arcseconds,  $r$  and  $\theta$  are the radial and the angular parts of the angular position on the sky, respectively, and  $\theta_\gamma$  is the position angle of the shear, measured East of North. The other is the Singular Isothermal Ellipsoid (SIE) model, with a projected potential of

$$\psi(r, \theta) = \alpha_e r [1 + ((1 - q^2)/(1 + q^2)) \cos 2(\theta - \theta_e)]^{1/2}, \quad (2)$$

where  $q$  is the lens axis ratio and the  $\theta_e$  is the position angle of the ellipse, measured East of North. Since component A is saturated in both the ACS F555W image and the F814W image, we adopted the positions and flux of components A and B in the MagIC image and the position of component G in the ACS (F814W) image. In order to obtain the position of G relative to A, we used the positions of components B and G in the ACS F814W image and the position angle of the ACS image, 120.37 degree. These observables are summarized in Table 1. We use the *lensmodel* software (Keeton 2001b) to model the lensed quasar system. Both mass models have eight parameters;  $\alpha_e, \gamma, \theta_\gamma$ , the lensing galaxy position, the source quasar position, and the source quasar flux for the SIS+shear model;  $\alpha_e$ , ellipticity  $e$  ( $e = 1 - q$ ),  $\theta_e$ , the lensing galaxy position, the source quasar position, and the source quasar flux for the SIE model. Since we have only eight constraints (positions of two lensed components and the lensing galaxy, and the fluxes of lensed components), the number of degrees of freedom is zero. The results are summarized in Table 3 and Table 4. The critical curve in the image plane and the caustics in the source plane of the SIS+shear model are shown in the left panel of Figure 10, and those of the SIE model are shown in the right panel of Figure 10, respectively. The best-fit models predict the time delay between the two lensed images to be  $\Delta t = 7.1h_0^{-1}$  day for the SIS+shear model and  $\Delta t = 8.9h_0^{-1}$  day for the SIE model ( $H_0 = 100h_0 \text{ km sec}^{-1} \text{ Mpc}^{-1}$ ), assuming that the redshift of the lensing galaxy is 0.724. Both the mass models predict the Einstein radius  $\alpha_e$  of about  $0''.55$ , which corresponds to the velocity dispersion (in one direction) of the lensing galaxy of  $\sigma \simeq 265 \text{ km sec}^{-1}$  at  $z = 0.724$ . Using the Faber-Jackson law (Faber & Jackson 1976),  $M_i^* = -21.3$  and  $\sigma^* = 225 \text{ km sec}^{-1}$  (Blanton et al. 2001; Kochanek 1996), and K- and evolution-correction for elliptical galaxies (Inada 2004; 1.0 and  $-0.1$ , respectively, derived from the model of Poggianti 1997 and the SDSS filter response function), the  $i$ -band magnitude of the lensing galaxy is predicted to be 22.1. This is in good agreement with the  $i$ -band magnitude of component G, 21.8. Thus these mass models further support that the redshift of the lensing galaxy is 0.724.

Although the number of degrees of freedom is zero in the above mass models, we were not able to reproduce the observables perfectly. The observed flux ratio between components B and A are  $\sim 0.33$ , while the predicted flux ratios are 0.58 for the SIS+shear model and 0.54 for the SIE model (see Table 3). The differences between the observed flux ratio and the predicted flux ratios are very large and therefore cannot be explained by the observed data errors. To explore the discrepancy, we speculate that an unknown object near component G (we named this *hypothetical* second lensing object “G’”) causes the discrepancy. In order to minimize the difference between the numbers of constraints and parameters, we simply applied the SIS model for both G and G’ (i.e., we did not consider the shear and the ellipticity). This model, however, has nine parameters and is under-constrained (the number

of the difference between the constraints and the parameters is 1), thus we required that the Einstein radius of  $G'$  should not be so large, smaller than  $\sim 0''.20$ ; this is natural since  $G'$  should not be the dominant contribution. We varied  $\alpha_e$  of  $G'$  between  $0''.01$  and  $0''.20$ , and search for the best-fit models for each value of  $\alpha_e$  of  $G'$ . We found that well-fitted models ( $\chi^2 \sim 0$ ) exist for each  $\alpha_e$  of  $G'$  between  $0''.05$  and  $0''.20$ . A result for the case that the Einstein radius of  $G'$  is  $0''.07$  is summarized in Table 3 and Table 4; the predicted flux ratio between components B and A is 0.33. If we simply apply the Faber-Jackson law, the Einstein radius of the SIS model is proportional to  $L^{1/2}$ ; thus that the Einstein radius of  $G'$  is  $0''.07$  corresponds to  $G' \sim 5$  mag fainter than G if we assume that  $G'$  is at the same redshift of G. This is consistent with the fact that we cannot see any objects at the predicted position of  $G'$  in the ACS images even after the PFS subtraction. The critical curve in the image plane and the caustics in the source plane of this model (2 SIS lens model for  $\alpha_e(G')=0''.07$ ) are shown in Figure 11, and the predicted time delay of this model is  $\Delta t = 8.7h_0^{-1}$  day. We note that the total magnification factors of all mass models (especially 2 SIS lens model) are much higher than those of the previously known two-image lensed quasars, e.g., HE1104–1805 (Wisotzki et al. 1993).

In the above lens models, it is expected that the shape of the lensed host galaxy, if it exists, is similar to that of the critical curve, because the quadruple moments are negligible and the source is close to the center of the lens system (Kochanek et al. 2001). To compare the ring feature observed in the NICMOS image and the critical curve of the best-fit mass model, we overplot the critical curve predicted by the 2 SIS lens model on the NICMOS ring, after subtracting the central lensing galaxy and excluding the pixels around components A and B. The result is shown in Figure 12. The red dot-dashed line in Figure 12 connects the pixels that have the maximum count rate in each column; thus it almost corresponds to the structure of the observed ring. In addition to the 2 SIS lens model, we also find that the critical curves of the SIS+shear model and the SIE model are in good agreement with the observed ring. A possible objection of this interpretation is that the magnification center of the observed ring is largely different from the center of component A in both the ACS and the NICMOS images; the ring might not be associated to the source quasar but be a background galaxy lensed by the same lensing galaxy.

#### 4. Summary and Conclusion

We have reported the discovery of the doubly-imaged gravitationally lensed quasar at  $z = 1.68$  with the separation angle  $1''.04$ , SDSS J0246–0825, which was selected from the SDSS data. The redshift of the lensing galaxy is likely to be  $z = 0.724$ , judged from the

absorption lines in the spectra of the quasar components and the apparent magnitude of the galaxy combined with the expected absolute magnitude from the Faber-Jackson relation.

We found that the simple mass models (SIS+shear and SIE) with reasonable parameters well reproduce the lensing geometry of SDSS J0246–0825 but do not reproduce the flux ratio between the lensed quasar components. Thus, we speculated that there is another lensing object near the lensed quasar system; we found possible lens models which can reproduce both the lensing geometry and the flux ratio, by introducing a faint second lensing object. All of the best fit models (including the SIS + shear model and the SIE model) predicts the time delay between the two lensed images to be  $\sim 10h^{-1}$  days. In addition to the two lensed images, we have found a highly distorted object in the *HST* ACS and NICMOS images. In particular, in the near infrared (NICMOS) image this object forms a nearly perfect ring. Since the critical curves of the best fit models show a good agreement with the ring, this is likely to be the lensed host galaxy of the source quasar.

A portion of this work was supported by NASA HST-GO-09744.20. N. I. and M. O. are supported by JSPS through JSPS Research Fellowship for Young Scientists. A portion of this work was also performed under the auspices of the U.S. Department of Energy, National Nuclear Security Administration by the University of California, Lawrence Livermore National Laboratory under contract No. W-7405-Eng-48. Some of the data presented herein were obtained at the W.M. Keck Observatory, which is operated as a scientific partnership among the California Institute of Technology, the University of California and the National Aeronautics and Space Administration. The Observatory was made possible by the generous financial support of the W.M. Keck Foundation.

Funding for the creation and distribution of the SDSS Archive has been provided by the Alfred P. Sloan Foundation, the Participating Institutions, the National Aeronautics and Space Administration, the National Science Foundation, the U.S. Department of Energy, the Japanese Monbukagakusho, and the Max Planck Society. The SDSS Web site is <http://www.sdss.org/>.

The SDSS is managed by the Astrophysical Research Consortium (ARC) for the Participating Institutions. The Participating Institutions are The University of Chicago, Fermilab, the Institute for Advanced Study, the Japan Participation Group, The Johns Hopkins University, the Korean Scientist Group, Los Alamos National Laboratory, the Max-Planck-Institute for Astronomy (MPIA), the Max-Planck-Institute for Astrophysics (MPA), New Mexico State University, University of Pittsburgh, University of Portsmouth, Princeton University, the United States Naval Observatory, and the University of Washington.

## REFERENCES

- Abazajian, K., et al. 2003, *AJ*, 126, 2081
- Abazajian, K., et al. 2004, *AJ*, 128, 502
- Bahcall, J. N., Maoz, D., Doxsey, R., Schneider, D. P., Bahcall, N. A., Lahav, O., & Yanny, B. 1992 *ApJ*, 387, 56
- Bergeron, J. 1988, *IAUS*, 130, 343
- Bergeron, J., & Boisse, P. 1991, *A&A*, 243, 344
- Bernstein, G. & Fischer, P. 1999, *AJ*, 118, 14
- Blanton, M. R., et al. 2001, *AJ*, 121, 2358
- Blanton, M. R., Lin, H., Lupton, R. H., Maley, F. M., Young, N., Zehavi, I., & Loveday, J. 2003, *AJ*, 125, 2276
- Browne, I. W. A., et al. 2003, *MNRAS*, 341, 13
- Chae, K.-H., et al. 2002, *Phys. Rev. Lett.*, 89, 151301
- Chiba, M. & Yoshii, Y. 1999, *ApJ*, 510, 42
- Clampin, M. et al. 2000, *SPIE*, 401, 344
- Eisenstein, D. J., et al. 2001, *AJ*, 122, 2267
- Faber, S. M. & Jackson, R. E. 1976, *ApJ*, 204, 668
- Fukugita, M., Futamase, T., & Kasai, M. 1990, *MNRAS*, 246, 24
- Fukugita, M., Shimasaku, K., & Ichikawa, T. 1995, *PASP*, 107, 945
- Fukugita, M., Ichikawa, T., Gunn, J. E., Doi, M., Shimasaku, K., & Schneider, D. P. 1996, *AJ*, 111, 1748
- Gunn, J. E., et al. 1998, *AJ*, 116, 3040
- Hogg, D. W., Finkbeiner, D. P., Schlegel, D. J., & Gunn, J. E. 2001, *AJ*, 122, 2129
- Impey, C. D., Falco, E. E., Kochanek, C. S., Lehar, J., McLeod, B. A., Rix, H.-W., Peng, C. Y., Keeton, C. R. 1998, *ApJ*, 509, 551

- Inada, N., et al. 2003a, *AJ*, 126, 666
- Inada, N., et al. 2003b, *AJ*, submitted
- Inada, N., et al. 2003c, *Nature*, 426, 810
- Inada, N. 2004a, PhD thesis, Department of Physics, University of Tokyo.
- Inada, N., et al. 2005, *PASJ*, in press
- Ivezić, Ž., et al. 2004, *AN*, 325, 583
- Johnston, D. E., et al. 2003, *AJ*, 126, 2281
- Keeton, C. R. 2001a, *ApJ*, 561, 46
- Keeton, C. R. 2001b, preprint (astro-ph/0102340)
- King, L. J., et al. 1998, *MNRAS*, 295, L41
- Kochanek, C. S. 1991, *ApJ*, 373, 354
- Kochanek, C. S. 1996, *ApJ*, 466, 638
- Kochanek, C. S., Keeton, C. R., & McLeod, B. A. 2001, *ApJ*, 547, 50
- Koopmans, L. V. E., & Treu, T. 2003, *ApJ*, 583, 606
- Koopmans, L. V. E., Treu, T., Fassnacht, C. D., Blandford, R. D., & Surpi, G. 2003, *ApJ*, 599, 70
- Krist, J. E. & Hook, R. N. 2003, *The Tiny Tim User's Guide, Version 6.1a*
- Lupton, R. H., Gunn, J. E., & Szalay, A. S. 1999, *AJ*, 118, 1406
- Lupton, R., Gunn, J. E., Ivezić, Z., Knapp, G. R., Kent, S., and Yasuda, N. 2001, in *ASP Conf. Ser. 238, Astronomical Data Analysis Software and Systems X*, ed. F. R. Harnden, Jr., F. A. Primini, and H. E. Payne (San Francisco: Astr. Soc. Pac.), p. 269 (astro-ph/0101420)
- Maoz, D., Bahcall, J. N., Doxsey, R., Schneider, D. P., Bahcall, N. A., Lahav, O., & Yanny, B. 1992, *ApJ*, 394, 51
- Maoz, D., Bahcall, J. N., Doxsey, R., Schneider, D. P., Bahcall, N. A., Lahav, O., & Yanny, B. 1993a, *ApJ*, 402, 69

- Maoz, D., et al. 1993b, ApJ, 409, 28
- Magain, P., Courbin, F., Sohy, S. 1998, ApJ, 494, 472
- Matthews, K., & Soifer, B. T. 1994, ASSL Vol. 190: Astronomy with Arrays, The Next Generation, 239
- Morgan, N. D., Snyder, J. A., & Reens, L. H. 2003, AJ, 126, 2145
- Myers, S. T., et al. 2003, MNRAS, 341, 1
- Ofek, E. O., Rix, H., & Maoz, D. 2003, MNRAS, 343, 639
- Oguri, M. 2002, ApJ, 580, 2
- Oguri, M., et al. 2004a, PASJ, 56, 399
- Oguri, M., et al. 2004b, ApJ, 622, 106
- Oke, J. B., & Gunn, J. E. 1983, ApJ, 266, 713
- Pier, J. R., Munn, J. A., Hindsley, R. B., Hennessy, G. S., Kent, S. M., Lupton, R. H., & Ivezić, Ž. 2003, AJ, 125, 1559
- Pindor, B., et al. 2004, AJ, 127, 1318
- Poggianti, B. M., 1997, *å*, 122, 399
- Refsdal, S. 1964, MNRAS, 128, 307
- Richards, G. T., et al. 2002, AJ, 123, 2945
- Richards, G. T., et al. 2004, ApJ, 610, 679
- Rusin, D., Kochanek, C. S., & Keeton, C. R. 2003, ApJ, 595, 29
- Sheinis, A. I., Bolte, M., Epps, H. W., Kibrick, R. I., Miller, J. S., Radovan, M. V., Bigelow, B. C., & Sutin, B. M. 2002, PASP, 114, 851
- Smith, A., et al. 2002, AJ, 123, 2121
- Spergel, D. N., et al. 2003, ApJS, 148, 175
- Stoughton, C., et al. 2002, AJ, 123, 485
- Strauss, M. A., et al. 2002, AJ, 124, 1810

Sutin, B. M. 1997, Proc. SIPE, 2871, 1116

Thompson, R. 1992, Space Science Reviews (ISSN 0038-6308), 61, no. 1-2, 69

Turner, E. L., Ostriker, J. P., & Gott, J. R., III 1984, ApJ, 284, 1

Turner, E. L. 1990, ApJ, 365, L43

Walsh, D., Carswell, R. F., & Weymann, R. J. 1979, Nature, 279, 381

Warren, S. J., Hewett, P. C., Lewis, G. F., Moller, P., Iovino, A., Shaver, P. A. 1996,  
MNRAS, 278, 139

Wisotzki, L., Koehler, T., Kayser, R., & Reimers, D. 1993, A&A, 278, L15

York, D. G., et al. 2000, AJ, 120, 1579

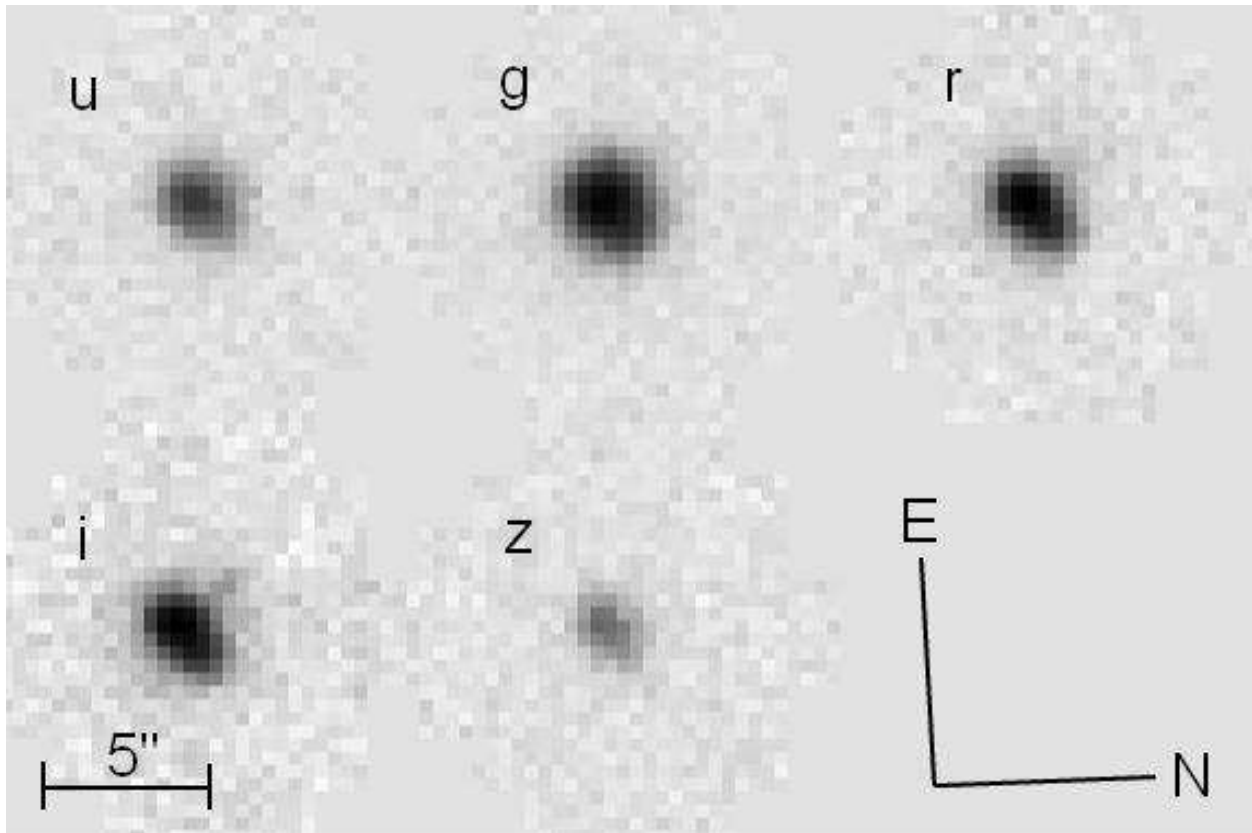


Fig. 1.— The images of SDSS J0246-0825 in all five SDSS bands (*ugriz*). The pixel size is  $0''.396$  and the seeing (FWHM) of the field was about  $1''.5$ . Total magnitudes in each band are 18.21, 17.99, 17.95, 17.60, and 17.58 in *u*, *g*, *r*, *i*, and *z*, respectively.

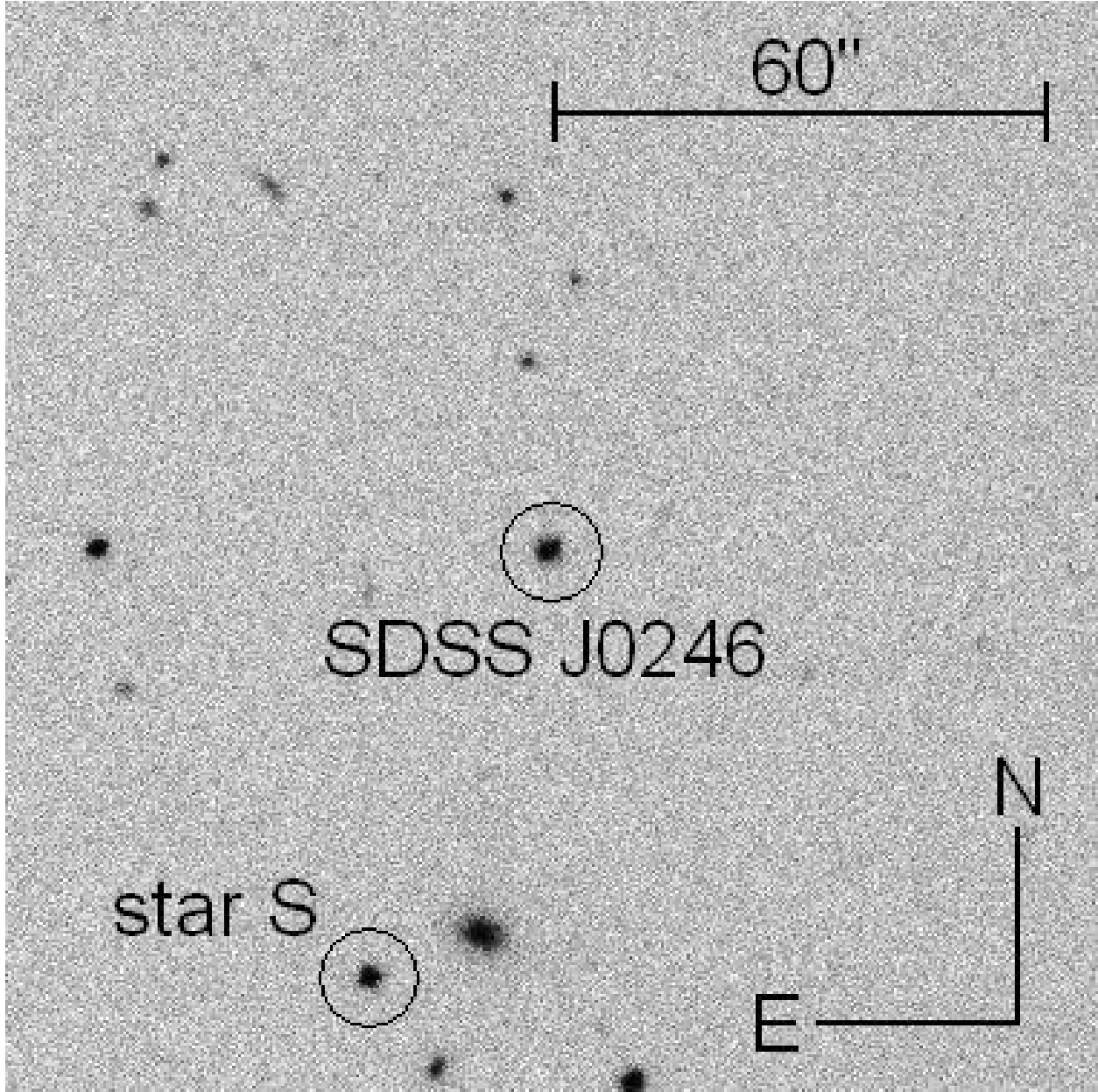


Fig. 2.— SDSS *i* band image of the field around SDSS J0246-0825. Star S, which is detected in both the WB6.5m data and the SDSS data, is used as a PSF template and a local photometric standard.

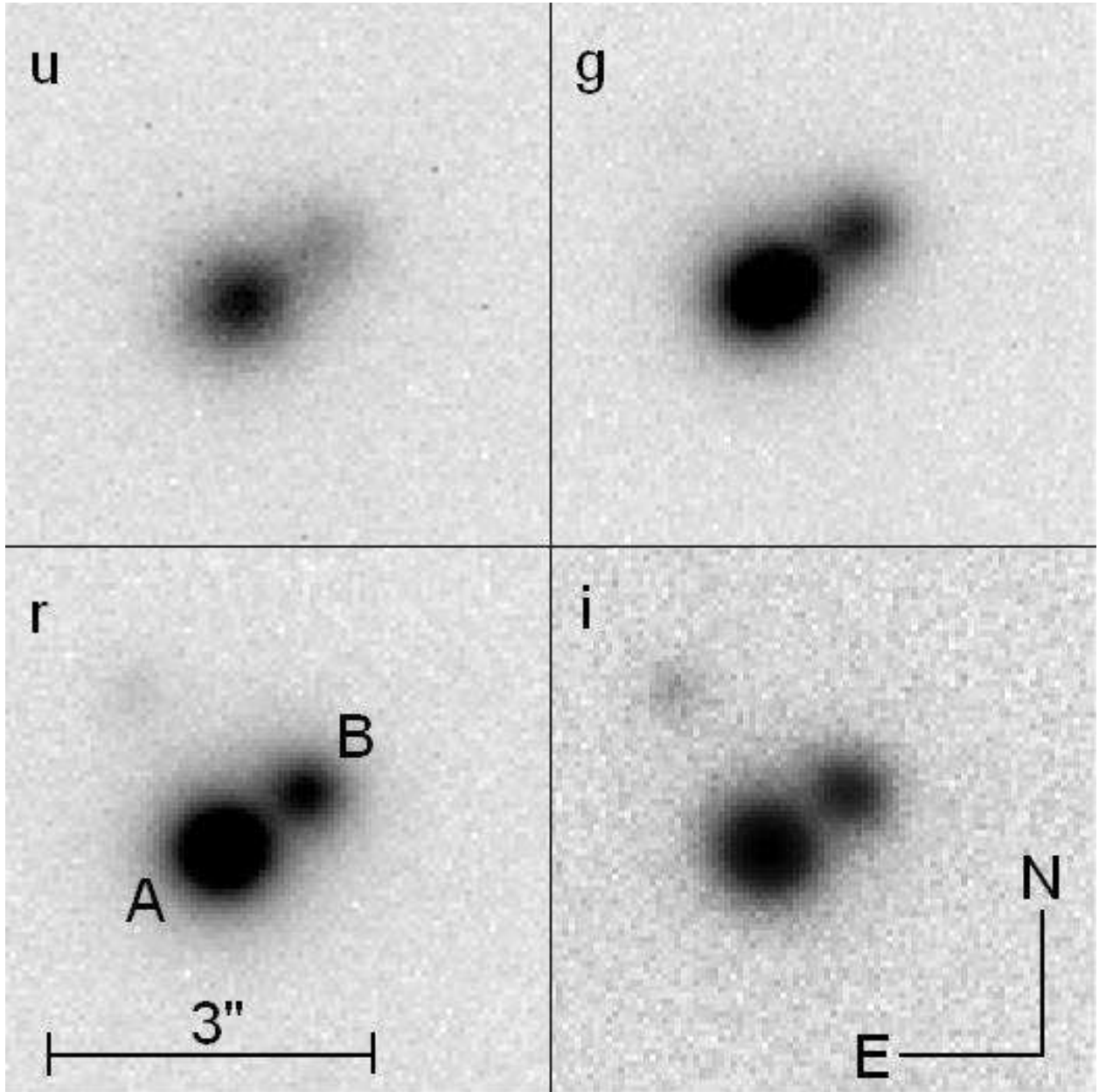


Fig. 3.— The MagIC images of SDSS J0246–0825 in *ugri* filters (appear as four separate images in this picture). Two stellar components are clearly seen in all images. The flux ratios between the two stellar components are 0.32, 0.31, 0.33, and 0.34 in *u*, *g*, *r*, and *i*, respectively. The separation angle between A and B is  $1''.042$  in the *i* band image. The pixel size of these images is  $0''.069$ , and the seeing (FWHM) was less than  $0''.6$ . The exposure time was 120 sec in each image.

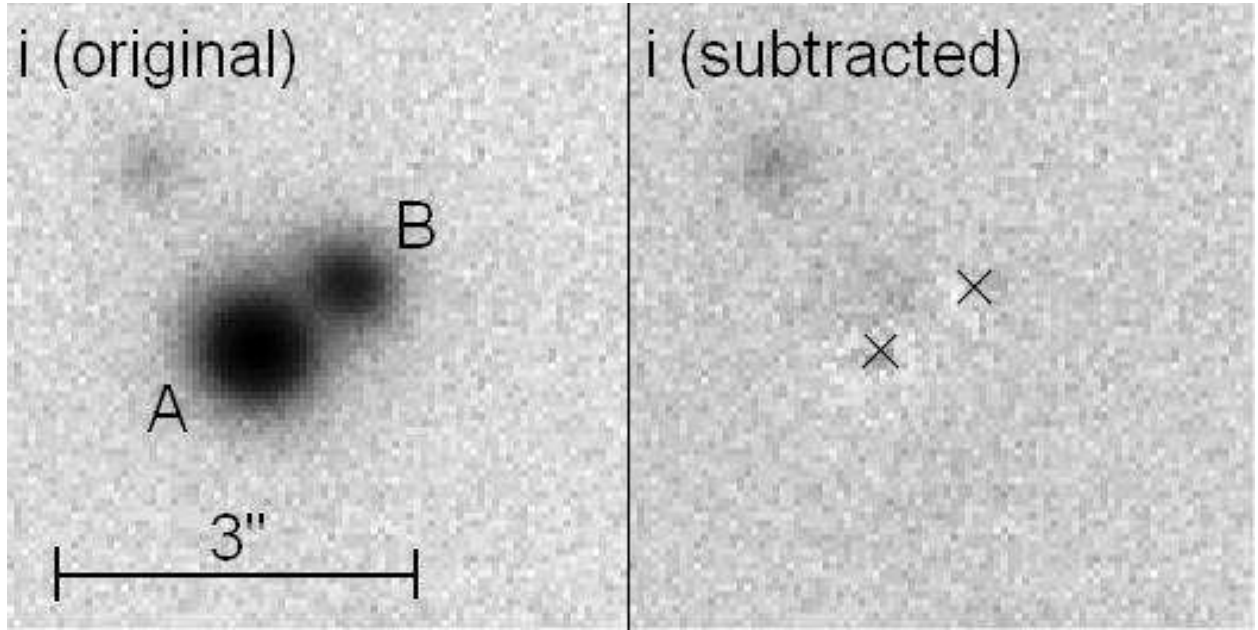


Fig. 4.— The MagIC  $i$  band image of SDSS J0246–0825 (*left*) and the PSF-subtracted image (*right*). The crosses in the right panels represent measured centers of components A and B. We find a faint, extended object ( $\sim 21.8$  mag in  $0''.5$  aperture radius) between the two stellar components (on the line between the two stellar components), although it is not obvious in this figure. The PSF magnitudes of components A and B are calculated to be 17.7 and 18.9, respectively.

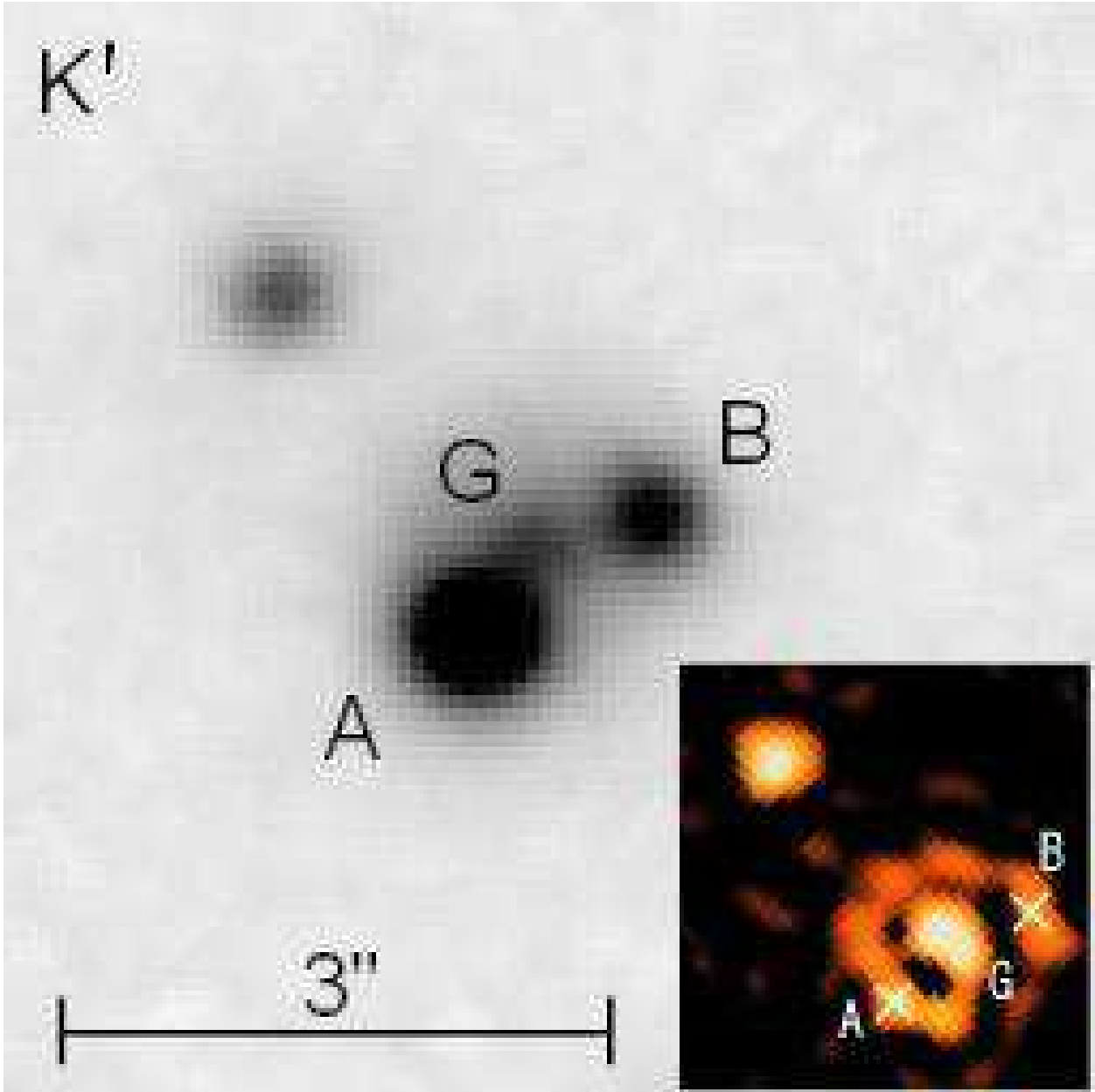


Fig. 5.— The deconvolved NIRC  $K'$  band image of SDSS J0246–0825. We can clearly see an extended object (component G) between components A and B. The position of this object agrees with that of the extended object found in the PSF-subtracted MagIC  $i$  band image. The flux ratio between components B and A (0.29) is consistent with the average of the optical bands (0.33). In the inset, we show the PSF-subtracted image (the crosses represent measured centers of components A and B).

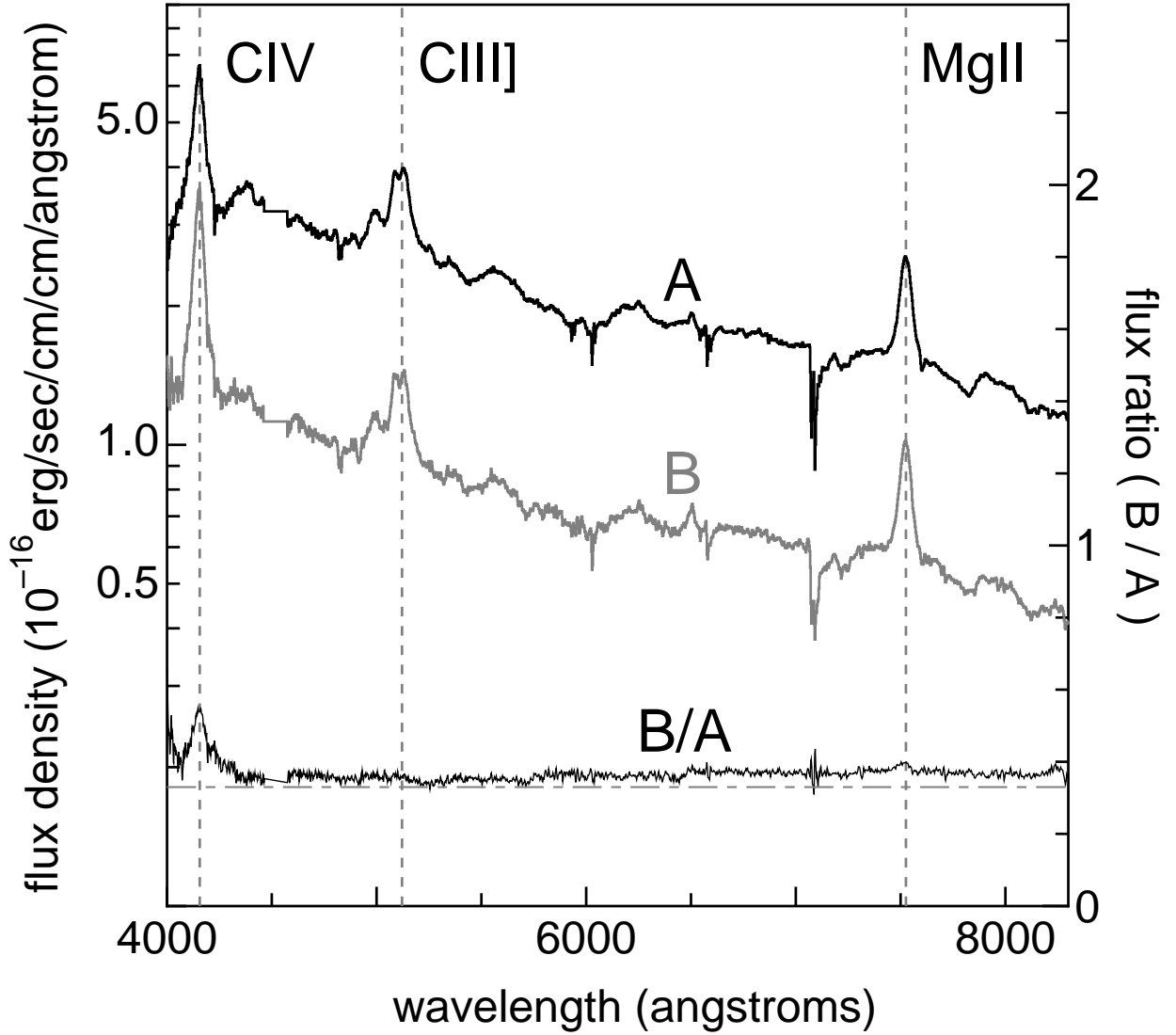


Fig. 6.— The (binned) spectra of SDSS J0246–0825 components A (black solid line) and B (gray solid line) taken with ESI on Keck II. The vertical grey dotted lines (4154.6 Å, 5119.2 Å, 7506.2 Å) represent the positions of emission lines red-shifted to  $z = 1.682$  of C IV (1549.06 Å), C III] (1908.73 Å), and Mg II (2798.75 Å), respectively. We find both components have C IV, C III], and Mg II emission lines at the same redshift ( $z = 1.68$ ). The bottom thin black solid line represents the spectral flux ratio between components B and A. The grey horizontal dot-dashed line represents the mean flux ratio (0.33) found in *ugri* photometry of the WB6.5m images. The spectral flux ratio is almost constant and consistent with the photometric flux ratio. The data between 4460 Å and 4560 Å were excluded due to the existence of the bad columns.

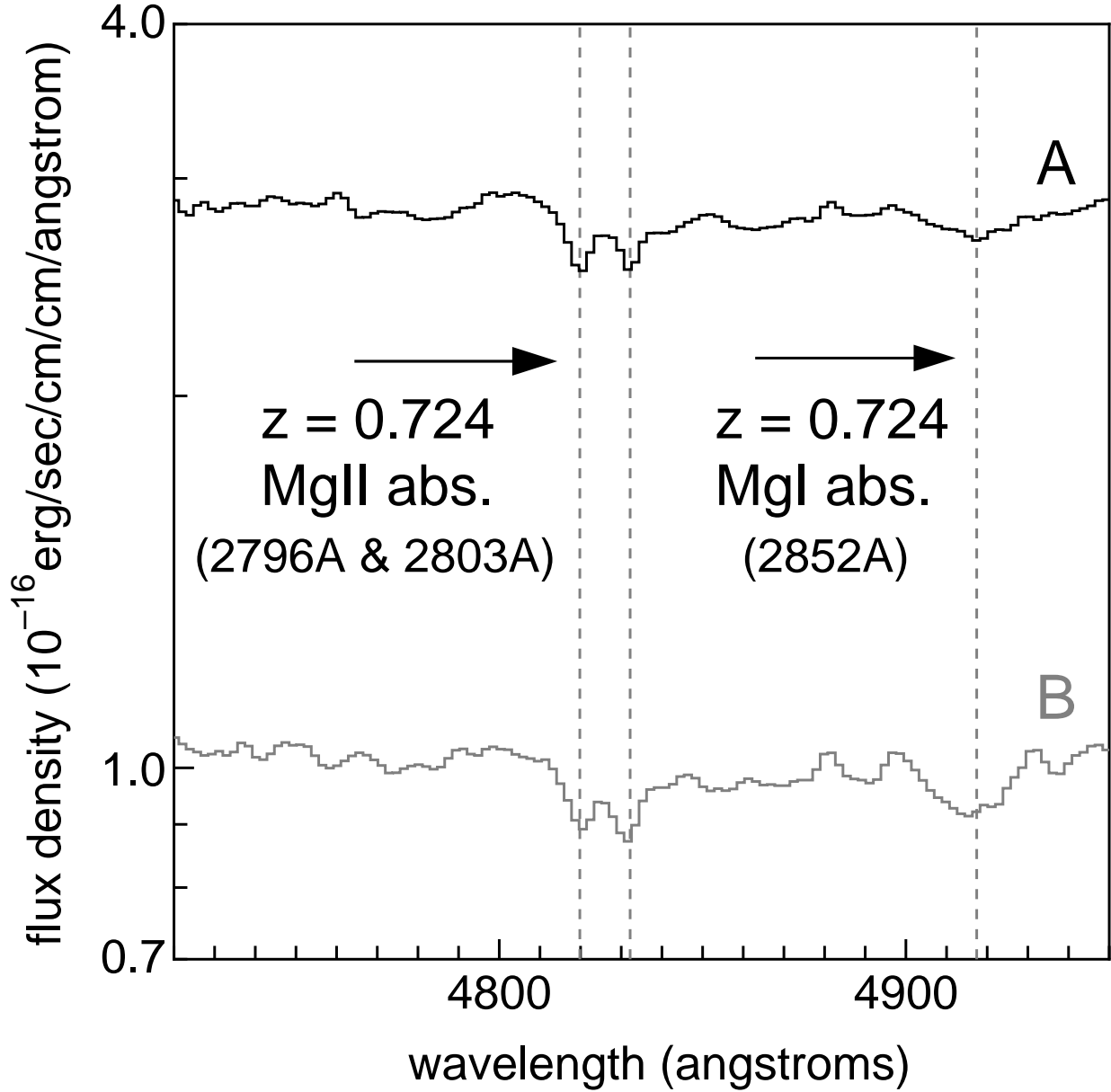


Fig. 7.— An enlarged region of Figure 6 showing the common absorption line features in SDSS J0246–0825 A and B. The vertical grey dotted lines (4819.5 Å, 4831.8 Å, and 4917.0 Å) represent the positions of absorption lines red-shifted to  $z = 0.724$  of Mg II (2795.53 Å & 2802.71 Å) and Mg I (2852.13 Å), respectively. The Mg II absorption lines and possibly the Mg I absorption line are seen in both components. The rest frame equivalent widths are 0.81 Å and 0.62 Å in the spectrum of component A, and 0.77 Å and 0.79 Å in the spectrum of component B, for Mg II 2795.53 Å and 2802.71 Å absorption lines, respectively.

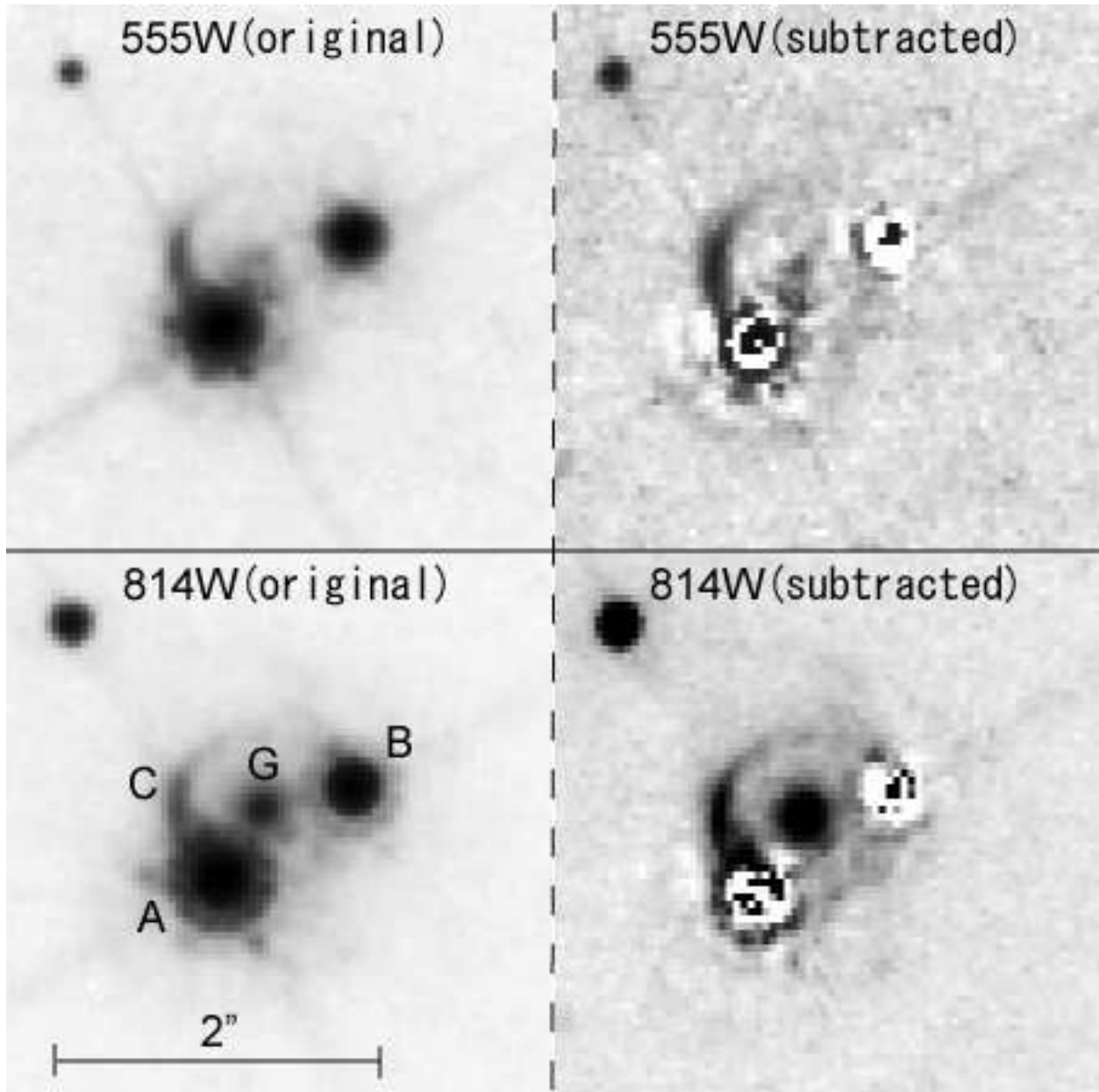


Fig. 8.— The ACS F555W image (*upper left*) and F814W image (*lower left*) of SDSS J0246–0825. Two quasar components are labeled A and B, and the central extended object is labeled G. The pixel scale is approximately  $0''.05 \text{ pixel}^{-1}$ . In addition to the central (lensing) galaxy, we find a highly distorted object (component C) near component A. The PSF-subtracted images of F555W and F814W filters are shown in the right panels (*upper right* and *lower right*, respectively). Note that component A is saturated in both the F555W filter and F814W filter images.

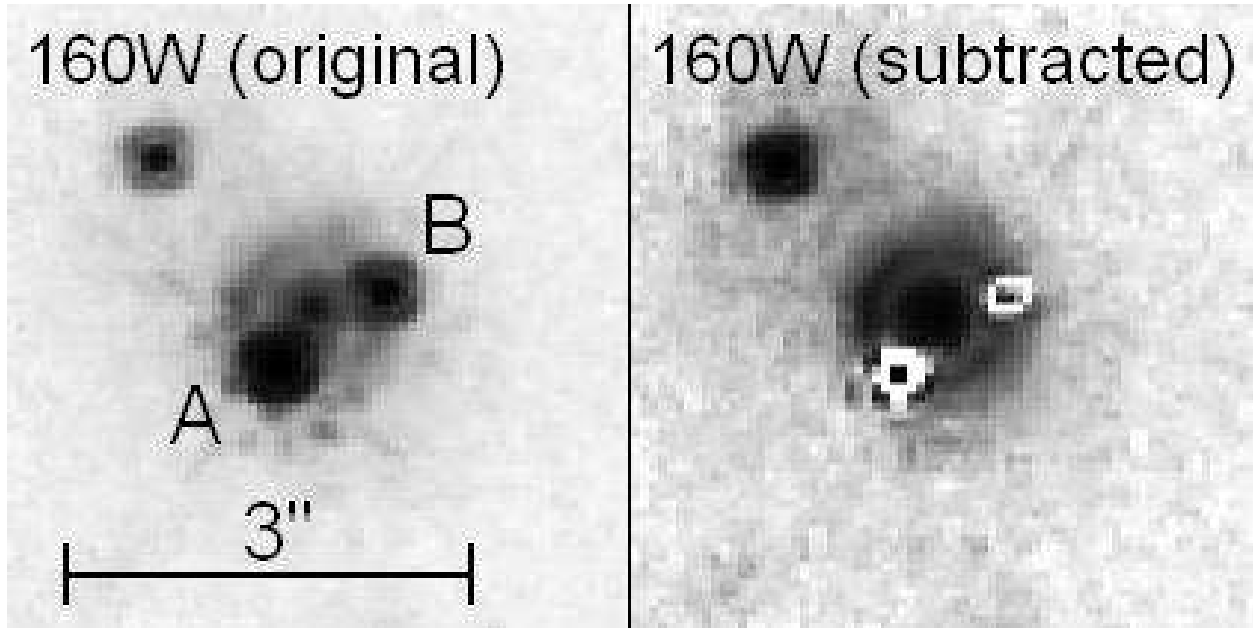


Fig. 9.— The NICMOS F160W image (*left*) and the PSF subtracted image (*right*) of SDSS J0246–0825. The pixel scale is approximately  $0''.075 \text{ pixel}^{-1}$ . The central extended object (component G) is clearly seen in both the original and the PSF subtracted image. We can see component C forms a nearly perfect ring in the PSF subtracted image. This ring feature is likely to be a lensed host galaxy of the source quasar (see Figure 12). The PSF magnitudes of components A and B are 17.3 and 18.6, respectively, and the aperture magnitudes ( $0''.375$  radius) of component G is 19.4.

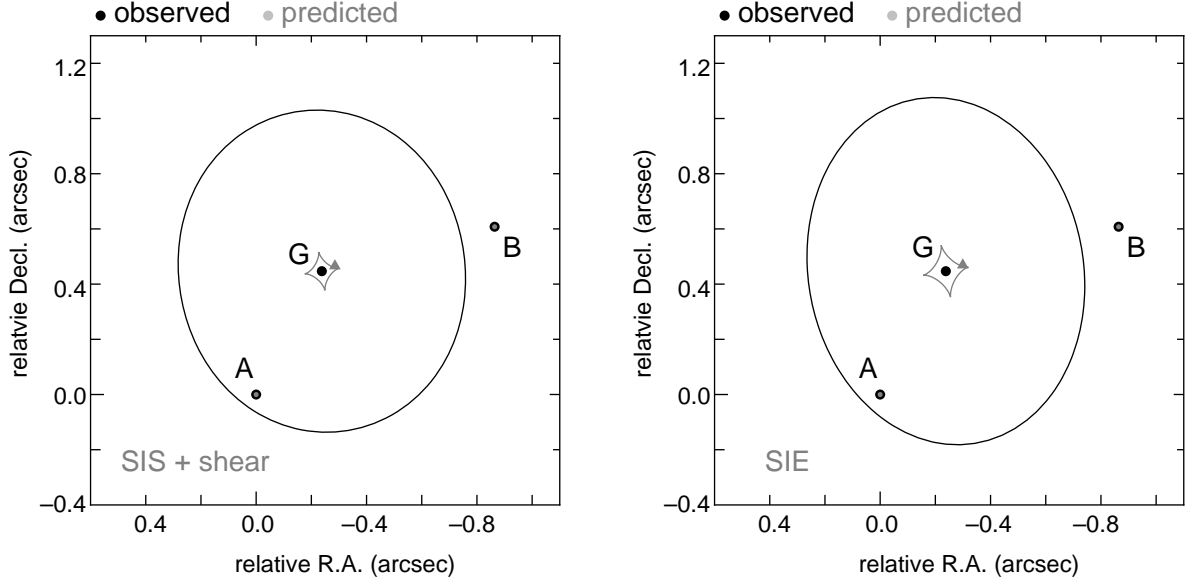


Fig. 10.— The critical curve (black solid lines) and the caustics (gray solid lines) of the best-fit SIS+shear model (*left* panel) and SIE model (*right* panel). The black filled circles represent the observed positions of the two lensed components (components A and B) and the lensing galaxy (component G). The gray filled circles represent the positions of the lensed components predicted by each mass model. The gray filled triangles are predicted source quasar positions. The best fit parameters for the SIS+shear model are  $\alpha_e = 0''.553$ ,  $\gamma = 0.067$ , and  $\theta_\gamma = 10.147^\circ$  with the source quasar position  $(\Delta\text{R.A.}, \Delta\text{Decl.}) = (-0''.285, 0''.466)$  relative to component A. The best fit parameters for the SIE model are  $\alpha_e = 0''.554$ ,  $e = 0.212$  ( $q = 0.788$ ), and  $\theta_e = 10.190^\circ$  with the source quasar position  $(\Delta\text{R.A.}, \Delta\text{Decl.}) = (-0''.299, 0''.469)$  relative to component A. Although the degree of freedom is zero in these models, both the mass models were not able to reproduce the observed flux ratio between components B and A.

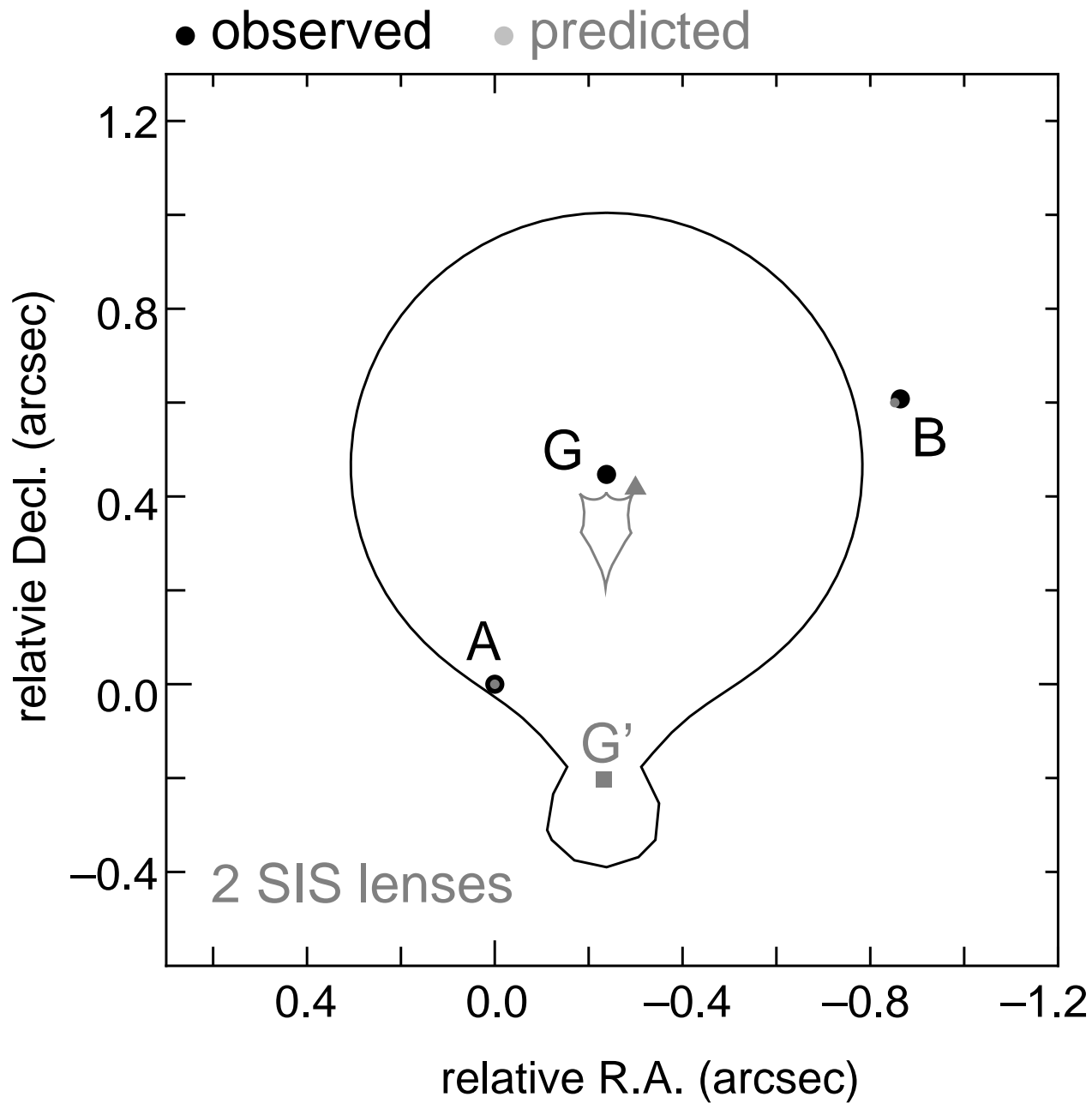


Fig. 11.— The critical curve (black solid lines) and the caustics (gray solid lines) of the 2 SIS lens model with  $\alpha_e(G')=0''.07$ . The gray filled square represents the position of the predicted second lensing object  $G'$ . The best fit parameters of this model are  $\alpha_e = 0''.525$  for component  $G$ , with the predicted position of  $G'$  ( $\Delta R.A., \Delta Decl.$ )= $(-0''.232, -0''.202)$  and the source quasar position ( $\Delta R.A., \Delta Decl.$ )= $(-0''.300, 0''.418)$ , relative to component  $A$ . This model reproduces the observed flux ratio,  $B/A=0.33$ .

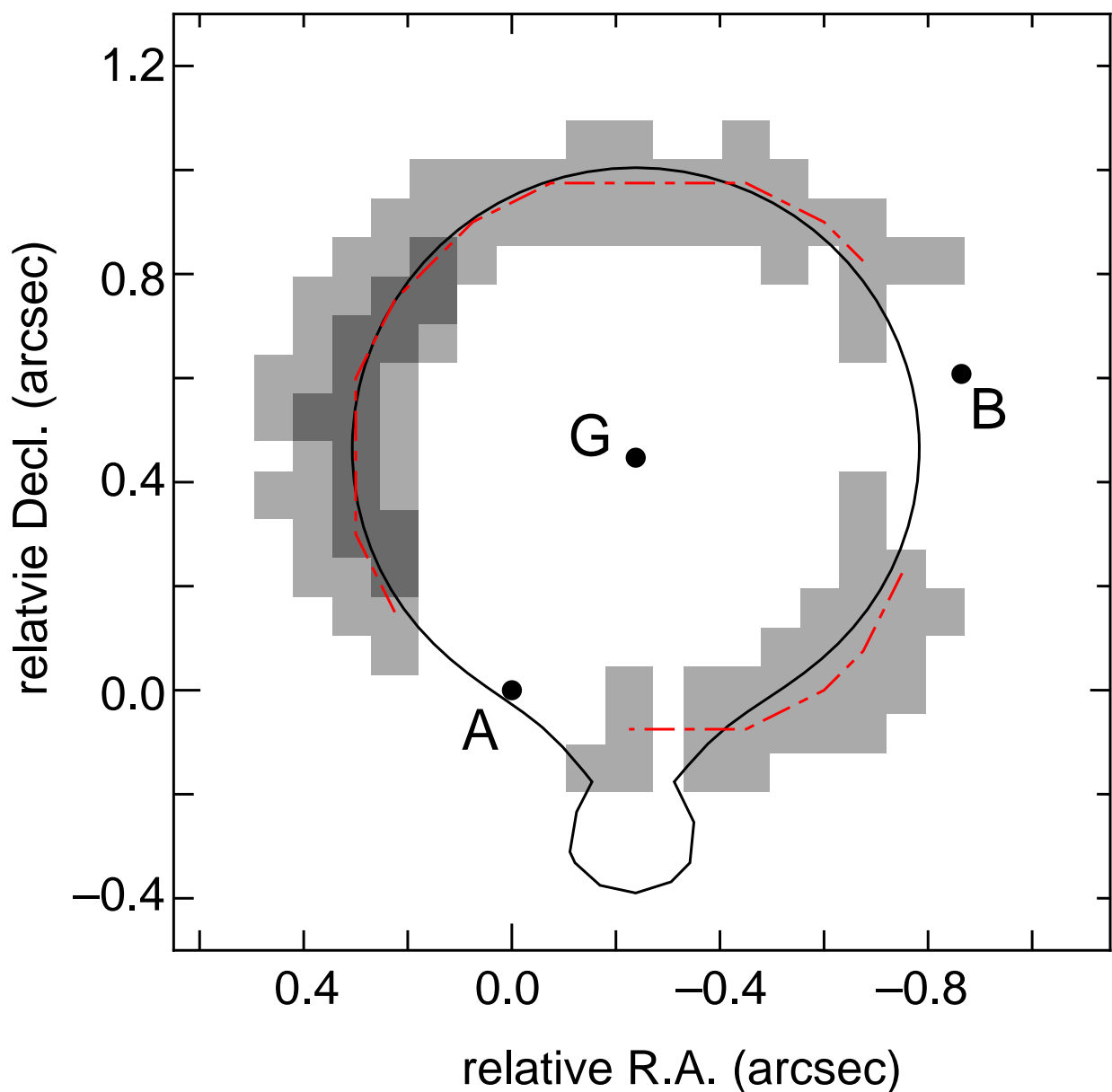


Fig. 12.— The comparison of the “ring” with the critical curve of the best-fit model. The solid line represents the critical curve predicted by the 2 SIS lens model with  $\alpha_e(G')=0''.07$ . The deep gray squares represent the pixels with higher count rate, after subtracting the central lensing galaxy and excluding the pixels around components A and B. The red dot-dashed line connects the pixels which have the maximum count rate in each column. The ring is in good agreement with the critical curve; this fact supports the idea that the ring is the lensed host galaxy of the source quasar.

Table 1. POSITIONS AND MAGNITUDES OF COMPONENTS OF SDSS J0246–0825

Object	$\Delta\text{R.A.}(\prime\prime)$ <sup>a</sup>	$\Delta\text{Decl.}(\prime\prime)$ <sup>a</sup>	$u$ <sup>b</sup>	$g$ <sup>b</sup>	$r$ <sup>b</sup>	$i$ <sup>b</sup>	F160W
Component A	$0.000\pm 0.001$	$0.000\pm 0.001$	$19.17\pm 0.05$	$18.73\pm 0.02$	$18.34\pm 0.02$	$17.94\pm 0.03$	$17.3\pm 0.1$
Component B	$-0.852\pm 0.001$	$0.600\pm 0.001$	$20.41\pm 0.10$	$20.00\pm 0.03$	$19.55\pm 0.03$	$19.11\pm 0.04$	$18.6\pm 0.2$
Component G	$-0.238\pm 0.002$	$0.447\pm 0.002$	...	...	...	$21.80\pm 0.60$	$19.3\pm 0.5$

<sup>a</sup>The celestial coordinates of component A is 024634.11–082536.3, J2000.

<sup>b</sup>The errors do not include the photometric uncertainty of the standard star.

Table 2. EMISSION LINES

Element( Å)	Component A			Component B		
	$\lambda_{obs}$ ( Å)	FWHM( Å)	Redshift	$\lambda_{obs}$ ( Å)	FWHM( Å)	Redshift
C IV(1549.06)	4154.56	69.5	1.6820±0.001	4153.97	68.7	1.6816±0.004
C III](1908.73)	5116.82	85.1	1.6807±0.003	5117.09	87.6	1.6809±0.004
Mg II(2798.75)	7524.94	65.8	1.6887±0.002	7524.07	64.7	1.6884±0.004

Table 3. RESULT OF LENS MODELING: I.

Model	$\alpha_e$	$\gamma$ or $e$	$\theta_\gamma$ or $\theta_e$	$\Delta$ R.A.(source)	$\Delta$ Decl.(source)	$\mu_{\text{tot}}$ <sup>a</sup>	B/A <sup>b</sup>	$\chi^2$ <sup>c</sup>
SIS+shear	0′553	0.067	10.147°	−0′285	0′466	13.9	0.58	4.70
SIE	0′554	0.212	10.190°	−0′299	0′469	12.4	0.54	3.64
2 SIS lenses	0′525	...	...	−0′300	0′418	32.7	0.33	0.16

<sup>a</sup>Predicted total magnification.

<sup>b</sup>Flux ratio between B and A.

<sup>c</sup> $\chi^2$  of model fitting. In model fitting, we assume slightly larger errors for the flux ratio (B/A) than the observed errors; 10% errors for SIS+shear and SIE and 5% errors for 2 SIS lenses.

Table 4. RESULT OF LENS MODELING: II.

Model	$\Delta$ R.A. (G)	$\Delta$ Decl.(G)	$\alpha_e$ (G′)	$\Delta$ R.A. (G′)	$\Delta$ Decl.(G′)
SIS+shear	0′238	0′447	...	...	...
SIE	0′238	0′447	...	...	...
2 SIS lenses	0′238	0′447	0′070	−0′232	−0′202